

Shear band broadening in simulated glassesDarius D. Alix-Williams¹ and Michael L. Falk^{1,2,*}¹*Department of Materials Science and Engineering, Johns Hopkins University, Baltimore, Maryland 21218, USA*²*Department of Physics and Astronomy, Department of Mechanical Engineering, Hopkins Extreme Materials Institute, Johns Hopkins University, Baltimore, Maryland 21218, USA*

(Received 5 July 2018; published 27 November 2018)

A model for shear band width as a function of applied strain is proposed that describes shear bands as pulled fronts which propagate into an unsteady state. The evolving structural state of material ahead of and behind the front is defined according to effective temperature shear-transformation-zone theory. The model is compared to another that is based on dimensional analysis and assumes shear band dynamics is governed by the strain rate within the shear band. These models are evaluated on three material systems: a two-dimensional binary Lennard-Jones glass, a $\text{Cu}_{64}\text{Zr}_{36}$ glass modeled using an embedded atom method potential, and a Si glass modeled using the Stillinger-Weber potential. Shear bands form in all systems across a variety of quench rates and appear to either broaden to the system size or saturate to a finite width, remaining contained within the simulation cell. The dimensional analysis-based model appears to apply only when band growth is uncontained, indicating the dominance of a single timescale in the early stages of shear band development. The front propagation model, which reduces to the dimensional analysis model, applies to both contained and uncontained band growth. This result suggests that competition between the rate of shear-induced configurational disordering and thermal relaxation sets a maximum width for shear bands in a variety of material systems.

DOI: [10.1103/PhysRevE.98.053002](https://doi.org/10.1103/PhysRevE.98.053002)**I. INTRODUCTION**

Strain localization, also known as shear banding, is a deformation mechanism present in a variety of amorphous systems including gels [1], granular media [2], and metallic glasses [3]. Despite the ubiquitous nature of shear bands, their phenomenological origins remain largely unknown [4]. Strain localization is often the precursor to brittle failure in systems such as metallic glasses, which limits the utilization of these materials as structural components [4]. In spite of their brittle nature, metallic glasses often have many desirable properties such as high strength-to-weight ratios and corrosion resistance [5]. By understanding how shear bands form, we could potentially engineer metallic glasses that avoid strain localization. Unfortunately, attempts to characterize the nature of shear bands in experimental systems have been limited by the small length and short timescales over which they form [3]. Simulation of shear bands presents an alternative method of studying this phenomenon.

In this study we propose a model for the time evolution of the width of a shear band as a function of applied strain in simulated glassy systems driven at constant strain rate in simple shear. This model assumes that shear bands are pulled fronts which propagate into an unsteady state. Effective temperatures characterize the structural states of material ahead of and behind the front, and these states evolve with strain according to effective temperature shear-transformation-zone (ET-STZ) theory. We refer to this model as the shear-transformation-zone pulled front (STZ-PF) model

and compare it to an existing model derived from dimensional analysis. The second model, originally developed by Jagla [6], assumes a single material length scale and that the strain rate within the shear band controls the timescale of material response. These assumptions result in a shear band width that is proportional to the square root of strain. We refer to this model as the shear band strain rate (SBSR) model.

We test the applicability of the SBSR and STZ-PF models to three simulated systems: a two-dimensional binary Lennard Jones glass, a three-dimensional embedded atom method $\text{Cu}_{64}\text{Zr}_{36}$ glass and a three-dimensional Stillinger-Weber Si glass. Three quench durations are used for each system yielding nine configurations. We generate multiple replicas of each configuration to reduce sample-to-sample variation. The geometry of the simulation and applied load is chosen such that shear bands form in all configurations. Two phenomena are observed: uncontained growth, where shear bands eventually envelope the entire simulation cell, or contained growth, where bands broaden to a fixed width.

A number of alternative frameworks for the deformation of amorphous solids exist and are able to recreate some aspects of the elastoplastic response shown in our simulations [6–9]. Some of these models [7,9] bear a number of similarities with ET-STZ theory, most notably the invocation of a dynamically varying “fictive temperature.” Where these models differ is in the particulars of how the structural state is defined and the resulting details of the dynamical equations.

This paper is arranged as follows. Under Sec. II, we introduce the concepts of effective temperature and shear transformation zones. We then detail the derivation of the linear spreading speed of a moving front propagating into an unsteady state based on an explicit form of the structural

*Corresponding author: mfalk@jhu.edu

evolution taken from ET-STZ theory. Under Sec. III, we outline how model systems were prepared and deformed as well as the procedure used to determine the width of the shear band. Under Sec. IV, we fit our models to simulation data and comment on the fit parameters they generate. Last, under Sec. V we summarize our work and comment on future directions.

II. THEORETICAL BACKGROUND

A. The shear band strain rate model

In deformed systems where strain localization dominates the response, Jagla proposed that a simple geometrical relationship is observed between the global strain rate, $\dot{\gamma}$, and the strain rate within the shear band, $\dot{\gamma}_b$ [6],

$$\dot{\gamma}_b = \frac{L}{w} \dot{\gamma}. \quad (1)$$

In this expression L is the length of the simulation cell perpendicular to the direction of the applied load and w is the width of the shear band.

If one assumes that the strain rate is the dominant timescale in such simulations, then we can justify the existence of a simple relationship between the rate of broadening of the shear band, \dot{w} , and the strain rate within the shear band:

$$\dot{w} = \frac{\mathcal{L}}{2} \dot{\gamma}_b, \quad (2)$$

where we introduce another length scale \mathcal{L} , which dictates the magnitude of broadening for a given configuration driven at constant strain rate. We surmise that this is a material length scale, with some dependence on the internal structure of the glass. A factor of 1/2 is included in Eq. (2) for convenience.

Taken together, these equations result in a simple analytic expression for the predicted width of a shear band as a function of applied strain:

$$w = \sqrt{w_0^2 + L\mathcal{L}(\gamma - \gamma_0)}, \quad (3)$$

where w_0 and γ_0 are the respective band width and strain at shear band nucleation. We will refer to this model as the SBSR model. The SBSR model suggests that, at sufficiently large applied strain, the width of the shear band is proportional to the square root of the applied strain, $w \propto \gamma^{1/2}$.

In the SBSR model the physics of the evolving glass is expressed using a single empirically determined parameter \mathcal{L} . This limits our ability to intuit response for a variety of glassy systems (metallic, covalent, etc.) or to draw connections between the response and the internal structure of a particular glass. To overcome these limitations, we seek an alternative expression for shear band broadening which incorporates the physics of ET-STZ theory, where a strong connection is drawn between material structure and response.

B. The shear-transformation-zone pulled front model derivation

We propose an alternative framework where band broadening is modeled as a pair of moving interfaces which separate jammed and flowing material inside and outside of the shear band. We assume that the leading edge of each interface, or front, moves outward at the linear spreading velocity v^* . This

velocity can be determined by linearizing the dynamical equations describing the state of material ahead of the front about the unsteady state. Our approach was adapted from a review of front propagation dynamics by W. van Saarloos [10].

In his review, van Saarloos defines *pulled fronts* as the class of interfaces whose propagation speed is exactly v^* in steady state. The speed of a growing and spreading perturbation, $u(x, t)$, can be characterized by constructing a level set line through this curve at some fixed, arbitrary value $u(x, t) = C$. The time-rate-of-change of the position of the intersection point of the line and the curve, $dx_c(t)/dt$, is expected to reach an asymptotic velocity, v^* as $t \rightarrow \infty$. This velocity can be calculated by linearizing the dynamical equations describing the structural state of the material ahead of the front and using a saddle-point approximation.

The details of this procedure are discussed extensively in Ref. [10]. In this subsection we first introduce effective temperature and shear transformation zones. These concepts are then combined in a dynamical model that describes the evolution of the structural state of our glassy systems. We linearize this model about a spatiotemporal perturbation to obtain a dispersion relation. The dispersion relation is analyzed at the saddle-point to find the linear spreading velocity, which is taken to determine the rate of band broadening. Finally, we find an analytic expression for the shear band width as a function of strain using this rate.

The concept of an effective temperature stems from the idea that nonequilibrium systems can be thought of as consisting of two, weakly coupled subsystems [4,11]. The first subsystem is what we traditionally imagine when referring to temperature and encompasses the fast kinetic or vibrational degrees of freedom that quickly come into equilibrium with the surroundings, while the second subsystem refers to the slow configurational degrees of freedom in the system. If one imagines a vitreous system surrounded by a reservoir that is quickly cooled from a high temperature above its melting point down to a temperature far below its glass transition temperature, at some point the slow subsystem and reservoir will fall out of equilibrium with each other, leaving the slow subsystem in a configuration on the potential energy landscape drawn from an ensemble typical of the glass transition temperature [12], often referred to as the fictive temperature. If we repeat this procedure at a slower cooling rate, then the system and reservoir remain in thermal equilibrium with each other for longer and fall out of equilibrium at a lower temperature. The slow subsystem of this second glass will have a configuration drawn from this lower temperature ensemble and will thus have a higher degree of structural order and a lower effective temperature.

In the ET-STZ theory it is proposed that when one does plastic work on such a glassy system nanoscopic defects called STZs undergo shear-induced structural rearrangements dissipating energy. A typical STZ contains ~ 100 atoms [13]. A simple model of STZs assumes that they have two states and, once rearranged, cease further transformation unless the direction of shear is reversed. For systems driven at constant strain rate, new STZs must be created via the dissipated plastic work to sustain the flow.

ET-STZ theory has undergone numerous changes and appeared in various forms since its introduction [11,14,15].

Our simulations are performed at finite temperature, therefore we desire a dynamical equation for the dimensionless effective temperature, χ , which includes the effects of shear-induced rejuvenation and thermal relaxation. We consider the shear banded system as spatially invariant in all but the y dimension, reducing shear band broadening to a spatially one-dimensional problem. At lower strain, shear bands can be spatially heterogeneous as evinced by various topological features and potential energy fluctuations. Shear bands become increasing homogeneous at higher strain, suggesting that effective temperature transport occurs in driven glassy systems. The dynamical equation for the evolution of the structural state should include a diffusive term to account for this effect.

We combine elements of STZ equations from two sources to achieve an expression for the evolution of the structural state of a deformed glassy system that incorporates changes due to both mechanical deformation and thermal relaxation. The effects of shear-induced disordering are sourced from an athermal study performed by Manning *et al.* [16]. A term for the thermal contribution is detailed by Langer [11]. A full derivation of our expression can be found in Appendix A. The dynamical equation for the evolution of the structural state is

$$\dot{\chi} = \frac{\epsilon_0 \chi}{\tilde{c}_0 \tau_0} \left\{ \frac{2}{\epsilon_0 s_0} s f(s) e^{-1/\chi} \left[1 - \frac{\chi}{\hat{\chi}} \right] + \kappa \rho(T) e^{-\beta/\chi} \left[1 - \frac{\chi}{\theta} \right] \right\} + l^2 \frac{2}{\tau_0} f(s) e^{-1/\chi} \frac{\partial^2 \chi}{\partial y^2}. \quad (4)$$

The first term in braces accounts for structural disordering due to mechanical work. Parameters χ and θ are the dimensionless effective and bath temperatures, respectively. It is assumed that the structural state of the shear-deformed system evolves towards an upper-limiting value $\hat{\chi}$. The parameter \tilde{c}_0 is a dimensionless specific heat; τ_0 is an internal timescale comparable to the phonon frequency, and ϵ_0 is a strain increment of order unity. STZ transitions occur when the deviatoric stress s surpasses the minimum flow stress s_0 at a rate proportional to $f(s)$. We hold off explicit definition of $f(s)$ until later in our derivation.

The second term in the braces in Eq. (4) represents the structural relaxation due to thermal fluctuations and consists of the following parameters: κ is a dimensionless scaling parameter, $\rho(T)$ is a thermal rate factor, and β is an activation term which dictates the susceptibility of STZ transitions to thermal fluctuations. The explicit form of $\rho(T)$ will not be detailed in this analysis. The final term of Eq. (4) allows the effective temperature to diffuse and contains a length scale l on the order of an STZ radius.

Prior studies [16] indicate that Eq. (4) is unstable to strain localization due to a nonlinear instability. However, the question we ask now is *Once this instability takes place, how does the resulting band broaden as material adjacent to the band is induced to flow along with the material in the initially nucleated band?* To answer this question, we refer to the literature on the propagation of fronts into unstable states [10], noting that the jammed material outside the band is unstable in the ET-STZ model. If we assume the propagation is consistent with a pulled front, then the unstable spreading speed can be obtained by analyzing the linear stability of the unstable state,

i.e., the material outside the band. To undertake this analysis, we decompose the structural state of the system far from the band into a spatially invariant term, $\chi_0(t)$, and some small perturbation $u(y, t)$, where $u \ll \chi_0$:

$$\chi(y, t) \equiv \chi_0(t) + u(y, t). \quad (5)$$

We give the perturbation the form $u = u_0 \exp(iky - i\omega t)$, a generic plane wave with amplitude u_0 , wave number k , and angular frequency ω . Parameters y and t represent position and time, respectively. The plane-wave equation is complex with imaginary number i . The evolution of the uniform part of the solution is

$$\dot{\chi}_0 = \frac{\chi_0 \epsilon_0}{\tilde{c}_0 \tau_0} \left\{ \frac{2}{s_0 \epsilon_0} s f(s) e^{-1/\chi_0} \left[1 - \frac{\chi_0}{\hat{\chi}} \right] + \kappa \rho(T) e^{-\beta/\chi_0} \left[1 - \frac{\chi_0}{\theta} \right] \right\}. \quad (6)$$

Since $u \ll \chi_0$, we can make the following approximations:

$$\exp\left(\frac{-1}{\chi_0 + u}\right) \approx \exp(-1/\chi_0) \left[1 + \frac{u}{\chi_0^2} \right], \quad (7)$$

$$\exp\left(\frac{-\beta}{\chi_0 + u}\right) \approx \exp(-\beta/\chi_0) \left[1 + \frac{\beta u}{\chi_0^2} \right]. \quad (8)$$

We now solve for the linear solution of \dot{u} , excluding any terms of order $O(\chi_0^{-2})$ or higher:

$$\dot{u} = \left\{ \frac{s}{s_0} \alpha f(s) - \tilde{\kappa} \right\} \frac{u}{\tau_0} + l^2 \frac{2}{\tau_0} f(s) e^{-1/\chi_0} \frac{\partial^2 u}{\partial y^2}. \quad (9)$$

In this expression α and $\tilde{\kappa}$ are rate factors that determine the magnitude of perturbation growth due to shear-induced disordering and structural relaxation, respectively. These rate factors are explicitly defined below.

The factor α has the following form:

$$\alpha = \frac{2}{\tilde{c}_0} \left(1 + \frac{1}{\chi_0} - \frac{1}{\hat{\chi}} - 2 \frac{\chi_0}{\hat{\chi}} \right) e^{-1/\chi_0}. \quad (10)$$

Recall that χ_0 characterizes the structural state of jammed material. There is a critical effective temperature χ_c beneath which a perturbation is expected to grow, i.e., for $\chi_0 < \chi_c < \hat{\chi}$. When the structural state of the jammed material exceeds this critical value, $\chi_0 > \chi_c$, a perturbation will decay. The parameter χ_c represents the crossover from heterogeneous to homogeneous deformation when thermal relaxation is ignored.

The rate factor $\tilde{\kappa}$ is

$$\tilde{\kappa} = -\kappa \rho(T) \frac{\epsilon_0}{\tilde{c}_0} \left(1 + \frac{\beta}{\chi_0} - \frac{\beta}{\theta} - 2 \frac{\chi_0}{\theta} \right) e^{-\beta/\chi_0}. \quad (11)$$

The term in parenthesis is always negative because $\theta \leq \chi_0 \leq \beta$ while all other terms are positive. A minus sign is introduced in order to yield a positive rate factor. A sign change also occurs in Eq. (9) and indicates that thermal relaxation dampens perturbations.

If we further assume that the stress in our systems is equal to the minimum flow stress, $s = s_0$, then we arrive at the

following:

$$\dot{u} = \frac{1}{\tau_0} (\alpha f(s_0) - \tilde{\kappa})u + l^2 \frac{2}{\tau_0} f(s_0) e^{-1/\chi_0} \frac{\partial^2 u}{\partial y^2}. \quad (12)$$

Recall that $u = u_0 \exp(iky - i\omega t)$. We can obtain the dispersion relation:

$$\omega = \frac{i}{\tau_0} \left[\alpha f(s_0) - \tilde{\kappa} - l^2 \frac{2}{\tau_0} f(s_0) e^{-1/\chi_0} k^2 \right], \quad (13)$$

where the spatial wave number k is complex and can be expressed as $k = k_r + ik_i$, where its real and imaginary components are denoted using subscripts r and i , respectively.

As discussed at length in Ref. [10], the linear spreading speed of the interface can be extracted from the dispersion relation via a saddle-point approximation. The k value of the saddle-point k^* and the linear spreading speed v_0^* are then given by Eq. (12) of Ref. [10]:

$$\left. \frac{d\omega}{dk} \right|_{k^*} = \frac{\omega_i(k^*)}{k_i^*}, \quad (14)$$

$$v_0^* = \frac{\omega_i(k^*)}{k_i^*}. \quad (15)$$

Equation (14) can be separated into its real and imaginary components and used to determine the critical wave number:

$$k^* = i \sqrt{\frac{\alpha f(s_0) - \tilde{\kappa}}{2l^2 f(s_0) e^{-1/\chi_0}}}. \quad (16)$$

The linear spreading speed is therefore:

$$v_0^* = 2\sqrt{2}l \frac{f(s_0)}{\tau_0} \sqrt{ae^{-1/\chi_0} \left(1 - \frac{\tilde{\kappa}}{\alpha f(s_0)}\right)}. \quad (17)$$

We assume that the STZ activation rate is proportional to the strain rate within the shear band:

$$f(s_0) \sim \frac{\tau_0 V}{2w} e^{1/\hat{\chi}}, \quad (18)$$

where V is the constant velocity imposed on the simulation cell at the boundary and w is the width of the shear band, and the density of STZs within the shear band is assumed constant and given by $\exp(-1/\hat{\chi})$. The rate of band broadening is therefore:

$$\dot{w} = 2v_0^* = 2\sqrt{2}l e^{1/\hat{\chi}} \sqrt{ae^{-1/\chi_0}} \frac{V}{w} \sqrt{1 - \frac{2\tilde{\kappa}w}{a\tau_0 e^{1/\hat{\chi}} V}}. \quad (19)$$

We define the dynamic length scale:

$$\mathcal{L} = 4\sqrt{2}l e^{1/\hat{\chi}} \sqrt{ae^{-1/\chi_0}} \quad (20)$$

that governs the initial rate of band broadening at low strain when $w \ll w_\infty$. This length scale appears in the SBSR model and is now explicitly defined in terms of the ET-STZ theory. Its functional form suggests that shear bands that arise within more disordered initial states broaden faster than bands that arise within less disordered initial states. Analysis of this expression is found in Appendix B.

We can also define a band width saturation length scale:

$$w_\infty = \frac{1}{2} \frac{a}{\tilde{\kappa}} \tau_0 V e^{1/\hat{\chi}}. \quad (21)$$

This length scale determines when the rate of shear band broadening goes to zero. The dependence of w_∞ on rate factors a and $\tilde{\kappa}$ suggests that it is set by the competition between shear-induced rejuvenation and thermally activated structural relaxation. Further analysis of the behavior of w_∞ is found in Appendix C.

Substitution of Eqs. (20) and (21) into (19) results in the following expression for the band broadening rate:

$$\dot{w} = \frac{\mathcal{L}V}{2w} \sqrt{1 - \frac{w}{w_\infty}}. \quad (22)$$

From this expression the aforementioned effects of \mathcal{L} and w_∞ are apparent. When $w \ll w_\infty$, the rate of band broadening is proportional to \mathcal{L} and inversely proportional to w and narrow bands are expected to grow faster than wider ones. As the band width approaches its saturation value, $w \rightarrow w_\infty$, the band growth rate is reduced to zero, $\dot{w} \rightarrow 0$.

The analytic solution to Eq. (22) is

$$\begin{aligned} & \left(2 + \frac{w}{w_\infty}\right) \sqrt{1 - \frac{w}{w_\infty}} - \left(2 + \frac{w_0}{w_\infty}\right) \sqrt{1 - \frac{w_0}{w_\infty}} \\ &= \frac{3}{4} \frac{\mathcal{L}V}{w_\infty^2} (t - t_0) = \frac{3}{4} \frac{\mathcal{L}L}{w_\infty^2} (\gamma - \gamma_0). \end{aligned} \quad (23)$$

In this expression, w_0 and γ_0 are the band width and global strain at shear band nucleation. We refer to this expression as the STZ-PF model. In the limit where $w_0 \ll w_\infty$ and $w \ll w_\infty$, $w^2 \approx w_0^2 + \mathcal{L}L(\gamma - \gamma_0)$, which is the same functional form as the SBSR model.

III. METHODS

A. System preparation

The shear band broadening models are tested on simulated glasses generated using LAMMPS [17]. Three systems are chosen to represent metallic and covalent glasses with planar geometry and correspond to a two-dimensional binary Lennard-Jones glass (LJ) [18], a three-dimensional $\text{Cu}_{64}\text{Zr}_{36}$ glass (CZ) modeled using an embedded atom method potential [19] and a three-dimensional silicon glass (Si) modeled with a Stillinger-Weber potential [20]. We restrict the depth of the CZ and Si systems in the z dimension such that they are effectively two dimensional. This simulation box depth is chosen to be larger than the cutoff of the respective interatomic potentials, as evinced by plotting the radial distribution functions (not shown) and observing that pair interactions are uncorrelated at this length. All simulations have a total of 80,000 atoms, an aspect ratio $L_x:L_y$ of 1:5, and periodic boundaries in all directions. Shear bands form in all systems when deformed in simple shear.

The LJ system was introduced by Lançon *et al.* in a study of phase stability of simulated quasicrystals [18] and shown to produce shear bands in previous studies [21]. We modify this system to include a pairwise interaction cutoff distance of 2.5σ . The length of the simulation cell perpendicular to the loading direction L is 639.5σ . There are 35,776 large and 44,224 small particles. We prepare three LJ configurations via a constant volume quench from a well-equilibrated liquid at $0.351 k_B/\epsilon$ to $0.0299 k_B/\epsilon$ over durations of 1000τ (LJ-1), $10,000 \tau$ (LJ-2), and $100,000 \tau$ (LJ-3). Temperature is

controlled using a Nose-Hoover thermostat [22]. We prepare 10 replicas for each configuration to minimize sample-to-sample variation. The internal structures of each LJ configuration are statistically different as indicated by their respective average potential energies: -2.15 eV (LJ-1), -2.17 eV (LJ-2), and -2.19 eV (LJ-3).

Preparation of the CZ system follows the work of Ding *et al.* [23]. We use an aspect ratio $L_x:L_y:L_z$ of 4:20:1 with $L_y = L = 502.98 \text{ \AA}$. Our system is composed of 28,800 Zr and 51,200 Cu atoms. Three CZ configurations are prepared through constant pressure quench from 2000 to 300 K at rates of 1.00 (CZ-1), 0.10 (CZ-2), and 0.01 (CZ-3) K/ps. Temperature and pressure are controlled using a Nose-Hoover thermostat and barostat. Five replicas of each configuration are prepared, with the average atomic energy of Cu atoms of -3.569 (CZ-1), -3.576 (CZ-2), and -3.589 (CZ-3) eV.

The final system is a silicon glass whose preparation was first introduced by Fusco *et al.* [24]. This system has a 4:20:1 aspect ratio with $L = 547.81 \text{ \AA}$ and 80,000 atoms. We prepared three configurations by quenching from 3500 K to 300 K at constant pressure using the Tersoff potential [25] and a Nose-Hoover thermostat and barostat. The quench rates were 0.100 K/ps (Si-1), 0.010 K/ps (Si-2), and 0.001 K/ps (Si-3). The system is subsequently annealed at 400 K for 100 ps using the Stillinger-Weber potential. Five replicas of each Si configuration are prepared with average potential energy values of -4.09 (Si-1), -4.10 (Si-2), and -4.11 (Si-3) eV.

B. Deformation

We deform our systems in simple shear by incrementally deforming the simulation cell at a constant rate of 0.0001 ps^{-1} (τ^{-1} , LJ). We integrate the SLLOD equations of motion [26,27] with fully periodic boundaries and velocity remapping for atoms which cross the periodic boundaries in the y direction. This shear protocol is consistent with Lees-Edwards boundary conditions [28]. Strain localization occurs in all simulations; however, the chosen geometry minimizes stress concentration allowing us to strain the systems in excess of 1000%. The systems are coupled to a Nose-Hoover thermostat at 300 K (CZ and Si) and $0.0299 k_B/\epsilon$ (LJ) to remove heat generated during shear.

Figure 1 shows stress-strain curves for a individual LJ, CZ, and Si configurations prepared at the slowest quench rate (duration, LJ). The shear stress has been normalized by the maximum value. In spite of their different interatomic potentials and dimensionality, all systems display linear-elastic behavior at low strain, followed by a transition to inhomogeneous deformation at their yield stress. A subsequent stress drop occurs once plastic deformation is accommodated by a shear band. The geometry of our simulations allow them to deform in excess of 1000% strain, as shown in the inset.

C. Measuring shear band width

Figure 2 is a schematic of the procedure used to approximate shear band width. We compute the local atomic strain using OVITO [29] with the initial, undeformed configuration as the reference state as shown in Fig. 2(a). A cutoff radius

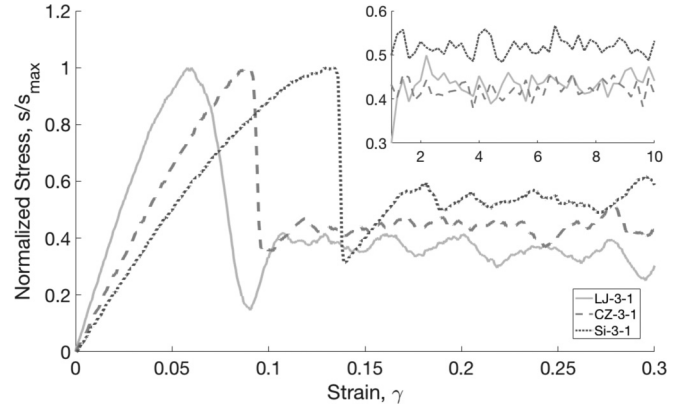


FIG. 1. Representative stress-strain curves for LJ (solid), CZ (dashed), and Si (dotted) systems. Shear stress has been normalized by the maximum stress and presented for strain from 0 to 30% (main) and 100 to 1000% (inlay). Data taken from a single simulation of the slowest-quenched configuration for a given system.

of 6 \AA (CZ and Si) or 2.2σ (LJ) is used to establish the neighborhood of each atom. The neighbor cutoff is chosen as roughly twice the distance to the highest peak of the radial distribution function. We interpolate the atomic strain onto a square grid of length 1 \AA (CZ and Si) or 1σ (LJ) using a natural method [30], as seen in Fig. 2(b). Next, a binary mask is applied to the grid which labels any square with an average atomic strain greater than or equal to 0.25 as one and all others zero. A feature is defined as a cluster of adjacent

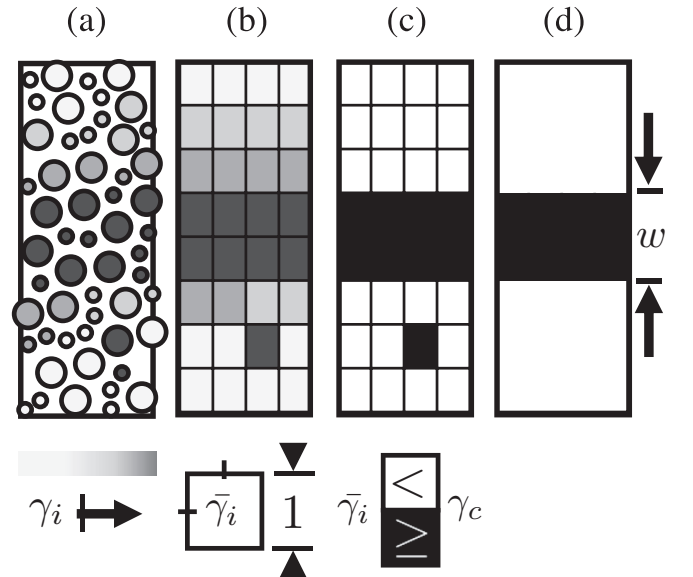


FIG. 2. Procedure for measuring shear band width. First we calculate per atom atomic strain γ_i , where i indexes over all particles (a). Strain is then averaged in regions of square length to determine $\bar{\gamma}_i$ (b). A binary mask is applied with cutoff $\gamma_c = 0.25$ and $\bar{\gamma}_i < \gamma_c \rightarrow 0$ and $\bar{\gamma}_i \geq \gamma_c \rightarrow 1$ (c). Contiguous squares are grouped as features with special attention paid to features which lie on the edges of the simulation cell. We treat the largest feature as the shear band and measure its height in the y direction to determine the band width w as a function of strain (d).

TABLE I. Simulation details for representative LJ configurations. Ten (10) simulations were performed for each configuration; however, simulations were excluded from the study if secondary shear bands formed during deformation.

Config. name	Quench duration (τ)	Average Atomic Energy (ϵ)	N
Lennard-Jones potential			
LJ-1	1e4	$-2.15 \pm .13$	6
LJ-2	1e5	$-2.17 \pm .12$	7
LJ-3	1e6	$-2.19 \pm .12$	10

ones and may cross the upper or lower cell bounds in the y direction. Figure 2(c) shows two clusters. We assume that the largest feature is the shear band and its width is measured by the average number of adjacent squares along the y direction, as in Fig. 2(d).

Shear bands are present in all systems by 20% deformation, as shown in Fig. 1. For simplicity, we use $\gamma_0 = 0.2$ as the global strain at band nucleation and measure the respective w_0 . Additional measurements are taken from strain of 100% onward at 100% strain increments. We limit our study to the broadening of a single shear band. Simulations are excluded from subsequent analysis if additional system-spanning features are present at any stage of the deformation, which would indicate the formation of a secondary shear band.

IV. RESULTS

The relative stability of a glass is measured by its average atomic energy and the likelihood that multiple shear bands will form increases with decreasing glass stability. Tables I and II list the average atomic energy and number of simulations considered for each configuration. For all systems, the first configuration is the least stable while the third configuration is the most stable due to its lower relative mean atomic energy. Consider the LJ system where 10 simulations are performed for each configuration. As LJ configurations are generated at slower quench rates, the mean atomic energy decreases and fewer simulations are excluded due to the formation of secondary shear bands. This trend is also observed

TABLE II. Simulation details for representative CZ and Si configurations. Five (5) simulations were performed for each configuration; however, simulations are excluded from our analysis if secondary shear bands form during deformation.

Config. name	Quench rate (K · ps)	Avg. potential energy (eV)	N
Embedded atom method potential			
CZ-1	0.100	$-3.57 \pm .07$	3
CZ-1	0.010	$-3.58 \pm .07$	5
CZ-1	0.001	$-3.59 \pm .07$	5
Stillinger-Weber potential			
Si-1	1.00	$-4.09 \pm .16$	4
Si-2	0.10	$-4.10 \pm .14$	5
Si-3	0.01	$-4.11 \pm .13$	5

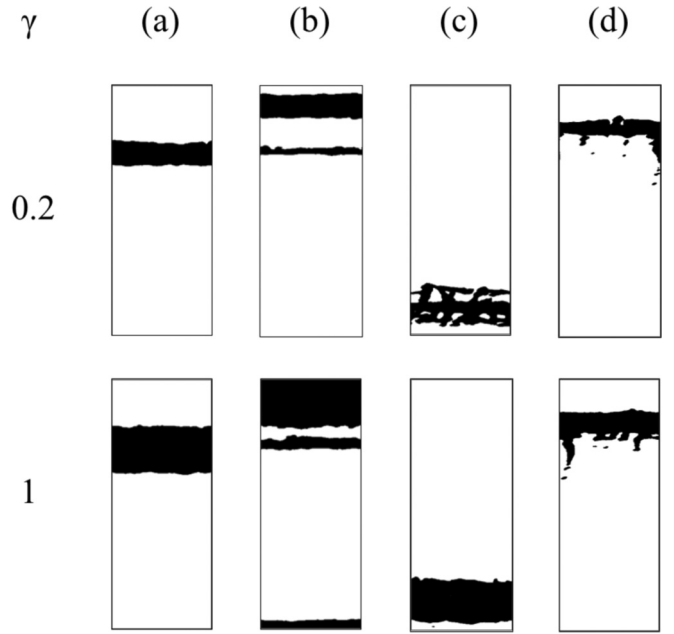


FIG. 3. High-strain material regions for multiple simulations when global strain is 20% (top row) and 100% (bottom row). Material regions with average atomic strain equal to or greater than 25% shown in black. Panel (a) is representative of the ideal case where a single, horizontal shear band forms. In (b) two shear bands are present, disqualifying this simulation from our analysis. The dominant feature in (c) has a porelike structure, with intermixed low- and high-strain material regions. The high-strain region of (d) features a large vertical component. Cases (a), (c), and (d) are included in our analysis.

in the CZ and Si systems, but secondary shear bands are more infrequent due to the need for instabilities to traverse both the width and depth of the three-dimensional simulation cell.

The SBSR and STZ-PF models assume that shear bands have well-defined edges and constant width; however, actual shear bands have more complex structures. Figure 3 shows several features for representative CZ [Figs. 3(a) and 3(b)] and LJ [Figs. 3(c) and 3(d)] simulations in black. These features correspond to regions where the average atomic strain is greater than or equal to 25% when the system is deformed to 20% shear strain (top row) and 100% strain (bottom row). The shear band shown in the CZ configuration [Fig. 3(a)] represents the ideal case where a single shear band forms and remains the dominant feature throughout the study.

In Fig. 3(b) a secondary shear band is present at 20% strain and broadening occurs in both features. Secondary bands may form at any stage of deformation and we exclude simulations from our analysis if they do. The formation of additional features indicates that in addition to aging, plastic deformation occurs in material outside the primary shear band. The STZ-PF model incorporates these effects by including a thermal relaxation term, κ and a structural rejuvenation term that depends on the local strain rate $\dot{\gamma}$.

Figures 3(c) and 3(d) shows shear bands with poorly defined edges due to intermixed regions of low strain. These porelike features occur most often in the two-dimensional LJ simulations at early stages of shear band formation ($\gamma \approx 20\%$)

TABLE III. Mean and standard deviation for SBSR and STZ-PF model parameters and R^2 values. Values are computed using fit data from N_s simulations where shear bands saturate to finite width w_∞ . Dimensionless lengths are reported by normalizing values by the system height L .

Config.	N_s	\mathcal{L}/L	R^2	\mathcal{L}/L	w_∞/L	R^2
LJ-1	6	0.018 ± 0.003	0.89 ± 0.08	0.034 ± 0.003	0.41 ± 0.03	0.99 ± 0.01
LJ-2	7	0.0069 ± 0.0008	0.94 ± 0.03	0.012 ± 0.001	0.27 ± 0.02	0.99 ± 0.01
LJ-3	7	0.0031 ± 0.0005	0.83 ± 0.19	0.006 ± 0.001	0.21 ± 0.16	0.97 ± 0.02
CZ-1	3	0.028 ± 0.002	0.98 ± 0.02	0.042 ± 0.005	0.69 ± 0.18	0.994 ± 0.005
CZ-2	4	0.0105 ± 0.0006	0.985 ± 0.004	0.014 ± 0.002	0.49 ± 0.15	0.995 ± 0.003
CZ-3	3	0.0019 ± 0.0003	0.70 ± 0.23	0.0037 ± 0.0004	0.138 ± 0.009	0.96 ± 0.03
Si-1	2	0.0108 ± 0.0007	0.967 ± 0.0004	0.017 ± 0.002	0.56 ± 0.19	0.988 ± 0.006
Si-2	5	0.0060 ± 0.0003	0.984 ± 0.007	0.0083 ± 0.0006	0.41 ± 0.05	0.997 ± 0.002
Si-3	3	0.0033 ± 0.0002	0.970 ± 0.01	0.0048 ± 0.0003	0.31 ± 0.03	0.997 ± 0.001

but are less pronounced at later stages of deformation. The coexistence of low- and high-strain regions within shear bands is less prevalent in CZ and Si simulations, which may be the result of averaging strain over the third dimension. We include simulations in the study when shear bands have rough edges (or vertical features), excluding only those in which additional, system-spanning features are present.

Vertical shear bands may occur at early stages of deformation as shown by the tail of the dominant feature in Fig. 3(d). These features persist in our simulations at 100% strain and dictate the preferred direction of band broadening. Vertical banding suggests that due to the symmetry of the deviatoric stress shear bands can form in both the horizontal and vertical directions. As the system is driven to higher strain large strains and the imposed boundary conditions break this symmetry causing STZ transitions to occur primarily along the horizontal band. The geometry of our simulation cell was

chosen to minimize these effects as a high aspect ratio favors horizontal banding.

Two scenarios are possible for simulations where a single shear band dominates the response: (1) uncontained growth, where the shear band widens to the extents of the simulation cell, or (2) shear band saturation, where broadening ceases and a shear band persists with finite width indefinitely on further deformation. A fit to the STZ-PF model is unable to determine a saturation length when $w_\infty \gg L$, thus we exclude cases of uncontained growth from our assessment of this model. Results reported in Table III are for N_s simulations, where subscript s represents the simulations where a finite saturation width is recovered.

Figure 4 plots band width as a function of global strain for the Si-1 configuration. Fits are performed for each simulation and average model parameter values are used to plot the STZ-PF (dashed line) and SBSR (dotted line) model results. Of

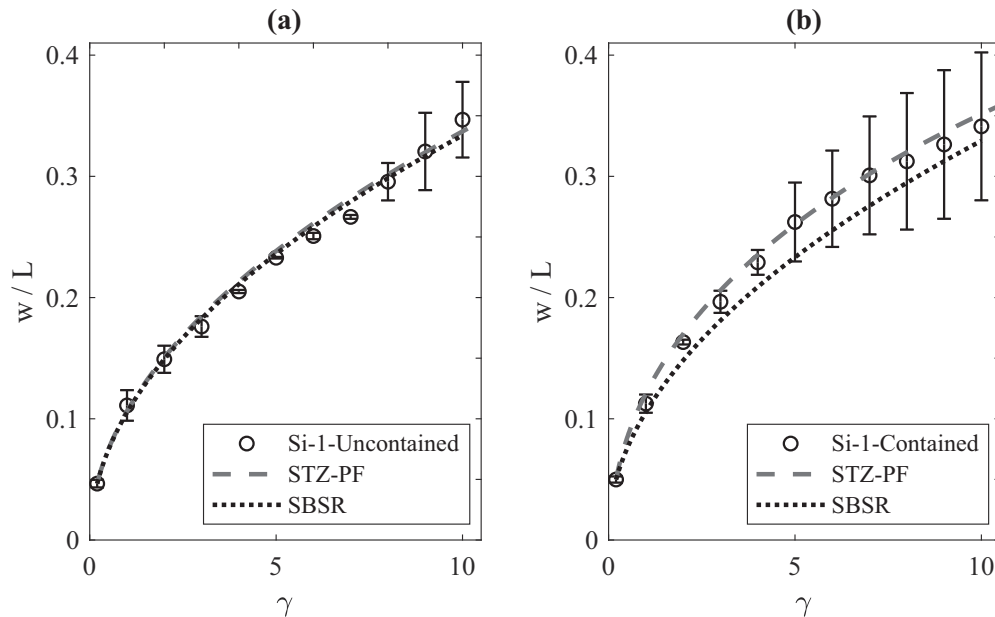


FIG. 4. Shear band width normalized by simulation height as a function of global strain for uncontained (a) and contained (b) Si-1 configuration simulations. A shear band is considered contained if the STZ-PF model fit yields a saturation width w_∞ that is less than the height of the simulation cell in the direction perpendicular to the applied strain, L , and uncontained otherwise. Standard deviation bars are shown. Average model parameters are calculated from fits to individual simulations and used to generate the STZ-PF (dashed) and SBSR (dotted) curves.

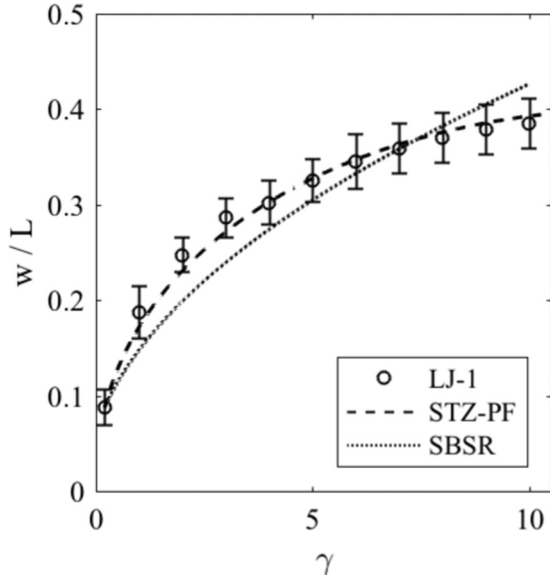


FIG. 5. Shear band width normalized by simulation height as a function of strain for LJ-1 configuration. Data averaged over six simulations where band growth is contained and $w_\infty < L$ in the STZ-PF model. Standard deviation bars shown. Simulations are independently fitted to STZ-PF and SBSR models and mean fit parameters are computed. The resultant STZ-PF (dashed) and SBSR (dotted) fits are plotted.

the five simulations performed, only two result in a persistent band of finite width, i.e., $w_\infty < L$. Figure 4(a) averages over the three Si-1 simulations where the STZ-PF model determines uncontained band growth. In this limit, w_∞ approaches infinity and the STZ-PF model reduces to the SBSR model. As expected, the SBSR and STZ-PF model fits coincide. In Fig. 4(b), models are compared for the remaining two Si-1 simulations where shear bands saturate. The STZ-PF model is far better at capturing the behavior of the Si-1 system at the low- and high-strain limits.

We use R -squared (R^2) as a metric for comparing the goodness of each model. We exclude simulations where uncontained growth is determined by the STZ-PF model because w_∞ is undefined. Table III provides average coefficient data as predicted by each model. These data are averaged over N_s configurations, where N_s is the number of simulations with a single, persistent shear band of finite width. In all cases the STZ-PF model provides marked improvement over the SBSR model. The SBSR model tends to underapproximate the dynamic length scale \mathcal{L} , which effectively determines the band width at low strain.

Figure 5 compares both models on the LJ-1 configuration where all simulations show contained band broadening, i.e., $N = N_s$. The slope of the SBSR curve at early strain is much smaller than that of the STZ-PF model. This is the result of the SBSR model having to strike a balance between accounting for the rapid increase in band width at low strain and the subsequent decrease and eventual plateau in band width at high strain. The addition of the saturation length scale in the STZ-PF model significantly enhances the estimation of band width and for the LJ-1 configuration the R^2 value increases from 0.89 (SBSR) to 0.99 (STZ-PF).

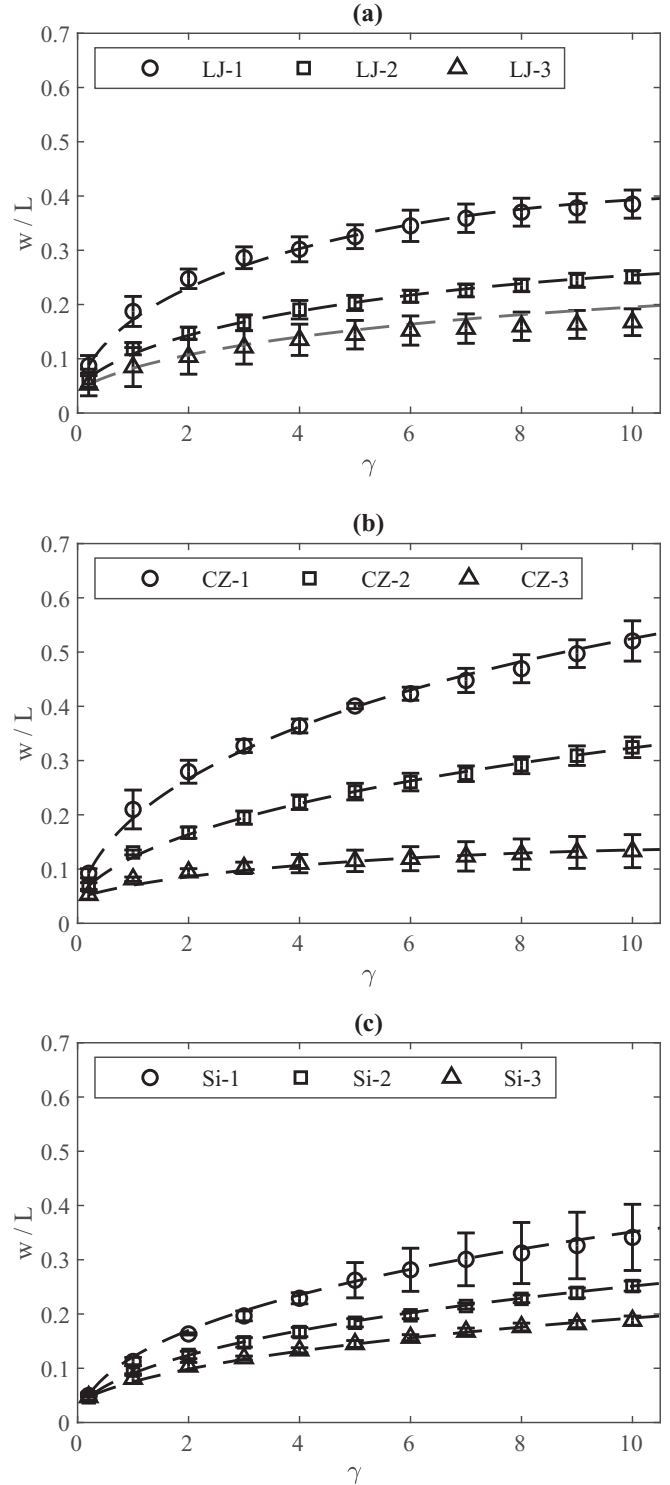


FIG. 6. Band width normalized by simulation height as a function of strain for LJ (a), CZ (b), and Si (c) systems. Data averaged over simulations where band growth is contained and $w_\infty < L$ in the STZ-PF model. Standard deviation bars shown. Circles represent fastest quench and triangles the slowest. STZ-PF model fit found by averaging over L and w_∞ values and shown by dashed line.

Shear band saturation is a ubiquitous phenomenon in the systems studied and occurs in the majority of simulations. In Fig. 6 we plot shear band width normalized by the height of the simulation cell as a function of applied strain for the

LJ (a), CZ (b), and Si (c) systems. Shapes correspond to configurations of a given system with circles indicating the fastest quench and triangles the slowest. Averages are taken over simulations where the STZ-PF model suggests band saturation with standard deviation bars shown. We assume that shear bands initiate at 20% strain and find that the initial width and dynamic length scale of the shear bands increases with increasing quench rate. The difference in initial band widths is less pronounced in the Si system where values are identical to within measured deviation. Saturation length also varies with quench rate with a larger width predicted for quickly quenched systems.

V. DISCUSSION

This study compares two models of shear band broadening—the shear band strain rate (SBSR) model which assumes that the rate of band broadening is proportional to the strain rate within the shear band and the STZ-PF model that describes shear band broadening as a pulled front propagating into an unsteady state. We test these models on three systems: a two-dimensional Lennard-Jones glass, a three-dimensional embedded atom method $\text{Cu}_{64}\text{Zr}_{36}$ glass, and a three-dimensional Stillinger-Weber silicon glass. Shear bands form in each system and their dynamics are well captured by the STZ-PF model, even when configurations are generated at increasingly high cooling rates.

The initial rate of shear band broadening is proportional to the strain rate within the band at low strain but deviates from this behavior at high strain as bands approach a saturation width. The SBSR model is able to capture the dynamics of shear bands at the onset of strain localization or whenever band width is uncontained by the simulation cell however, the SBSR model breaks down as shear bands approach their limiting width. The STZ-PF model improves on this shortfall in the SBSR model by introducing a band width saturation length scale that depends on the internal structure and rate of thermal relaxation of the glass. The STZ-PF model reduces to the SBSR model whenever band width is much smaller than saturation length, such as the case of uncontained band growth.

Shear band saturation is observed in various simulations produced with different interatomic potentials, dimensions and quench schedules. We argue that the saturation length scale is a ubiquitous feature of sheared amorphous systems. Glassy configurations are generated by sampling from a distribution of structures in a potential energy landscape which results in systems of the same potential, composition and preparation having a distribution of saturation band widths. In select simulations, the observed uncontained growth and the inability of the STZ-PF model to recover this length scale can be attributed to a simulation size that is less than the saturation width.

This work represents the first step in an ongoing study of strain localization in simulated glasses. It demonstrates that the structural state of sheared glassy systems can be well-described using an effective temperature and the dynamics of the state can be described using ET-STZ theory. Our results suggest that shear bands can be modeled as pulled fronts

which propagates into an unsteady state. The dynamics of the state on either side of the front can be described as a competition between increasing structural disorder due to plastic work and increasing structural order due to thermal relaxation.

Experimental studies of shear banding in metallic glasses report widths ranging from 10 to 210 nm [31] while our STZ-PF model predicts band widths between 6.9 (CZ-3) and 34.7 (CZ-1) nm. Although these results seem promising, we acknowledge several difficulties when drawing comparisons between simulated and experimental systems. The simplified geometry of our simulations allows them to deform to strains typically unobservable in experimental systems, where stress concentration often leads to catastrophic failure before a steady-state flow stress is achieved. Our simulations are effectively two dimensional and our analysis is done in one dimension. In contrast, experimental systems have finite depth and bands must broaden both perpendicular to the loading direction and along this depth. The length and timescales of simulations and experiments vary by orders of magnitude. Experimental systems have length scales of millimeters and timescales of milliseconds while our simulations are on scales of nanometers and nanoseconds respectively.

This preliminary study leaves many questions unanswered. A subsequent investigation will focus on understanding the role of thermally induced structural relaxation by shearing LJ glasses at different bath temperatures. We predict that as the reservoir temperature increases, thermal relaxation should play a larger role in the material response, leading to a decrease in saturation length. This study should provide insight into the functional form of κ . Several model parameters depend explicitly on the structural state of the system, which is poorly defined. We also hope to elucidate the relationship between potential energy and effective temperature in order to quantify χ and completely define our systems in terms of ET-STZ theory.

ACKNOWLEDGMENTS

This work was supported through NSF Award No. DMR 1408685/1409560. This research was also supported in part by the NSF under Grant No. NSF PHY17-48958. The authors also acknowledge helpful conversations with James Langer, Robert Maaß, Sylvain Patinet, and Mark Robbins.

APPENDIX A: DERIVATION OF THE EFFECTIVE-TEMPERATURE DYNAMICAL EQUATION, $\dot{\chi}$

The general structure for the evolution of the effective temperature proposed by Manning *et al.* in Ref. [16] equation (A5) is

$$\dot{\chi} = \frac{1}{C_{\text{eff}} T_Z} \left\{ T_{\text{eff}} \left(\frac{dS_C}{dt} \right)_{\text{mech}} \left[1 - \frac{\chi}{\tilde{\chi}} \right] + T_{\text{eff}} \left(\frac{dS_C}{dt} \right)_{\text{therm}} \left[1 - \frac{\chi T_Z}{T} \right] \right\} + D \frac{\partial^2 \chi}{\partial y^2}. \quad (\text{A1})$$

In this expression C_{eff} is a specific heat and $T_Z = E_Z/k_B$, where E_Z is the energy required to nucleate a STZ and k_B is the Boltzmann constant.

Heat due to mechanical work done on the system, $T_{\text{eff}}(dS_C/dt)_{\text{mech}}$, drives the structural state, $\chi = T_{\text{eff}}/T_Z$, towards the steady-state value $\hat{\chi}$. The existence of $\hat{\chi}$ has been demonstrated in a prior study of the LJ system [21] where a linear relation was assumed between effective temperature and potential energy and the average potential energy of material within the shear band was found to converge to a fixed value. Conversely, heat generated from thermal fluctuations, $T_{\text{eff}}(dS_C/dt)_{\text{therm}}$, relaxes the structural state towards the bath temperature T . We introduce a dimensionless bath temperature $\theta = T/T_Z$, analogous to the dimensionless effective temperature. A final term allows structural disorder to diffuse. We assume the rate of diffusion is governed by the plastic strain rate $\dot{\gamma}$ yielding a coefficient, $D = l^2|\dot{\gamma}|$, where l is a length scale on the order of a STZ radius. The equation for the plastic strain rate is

$$\dot{\gamma} = \frac{2}{\tau_0} f(s) e^{-1/\chi}. \quad (\text{A2})$$

The parameter τ_0 is an internal timescale comparable to the phonon frequency and $f(s)$ is a function of the deviatoric shear stress, s . The plastic strain rate is the product of the rate of stress induced STZ transitions, $2f(s)/\tau_0$, and an Arrhenius term that is proportional to the number density of STZs, $\exp(-1/\chi)$. It is assumed that STZ transitions occur only in the direction of loading. We hold off providing an explicit definition of $f(s)$ until later in our derivation.

In Ref. [16], Eq. (A13), Manning *et al.* provide an expression for the rate of configurational entropy production due to mechanical loading:

$$\left(\frac{dS_C}{dt}\right)_{\text{mech}} = \frac{k_B v_Z \epsilon_0}{\Omega \tau_0} \Lambda \Gamma(s), \quad (\text{A3})$$

where v_Z is the number of molecules within an STZ, Ω is the volume per molecule, ϵ_0 is a strain increment of order unity, $\Lambda = \exp(-1/\chi)$ is proportional to the STZ density, and $\Gamma(s)$ is the energy dissipated per STZ.

Equation (A10) of Ref. [16] provides the STZ energy dissipation term:

$$\Gamma(s) = \frac{2}{s_0 \epsilon_0} s f(s), \quad (\text{A4})$$

where s_0 is the minimum flow stress and s is the deviatoric shear stress.

Combining Eqs. (A3) and (A4),

$$\left(\frac{dS_C}{dt}\right)_{\text{mech}} = \frac{k_B v_Z \epsilon_0}{\Omega \tau_0} e^{-1/\chi} \frac{2}{s_0 \epsilon_0} s f(s). \quad (\text{A5})$$

Manning *et al.* analyze strain localization simulations performed at low temperature and assume that the contribution due to thermal fluctuations is marginal. Consequently, an expression for $(dS_C/dt)_{\text{therm}}$ is not provided. We refer instead to Ref. [11], Eq. (6.2), where Langer suggests the following form:

$$\left(\frac{dS_C}{dt}\right)_{\text{therm}} = \kappa \frac{k_B v_Z \epsilon_0}{\Omega \tau_0} \rho(T) e^{-\beta/\chi}. \quad (\text{A6})$$

In this expression κ is a dimensionless scaling parameter, $\rho(T)$ is a thermal factor whose form is beyond the scope of this derivation, and β is an activation term which dictates the susceptibility of STZ transitions to thermal fluctuations.

Manning *et al.* define a dimensionless effective temperature $\tilde{c}_0 = C_{\text{eff}} \Omega / (k_B v_Z)$. Combining Eqs. (A1)–(A6), the evolution of the structural state is expressed as

$$\dot{\chi} = \frac{\chi \epsilon_0}{\tilde{c}_0 \tau_0} \left\{ \frac{2}{s_0 \epsilon_0} s f(s) e^{-1/\chi} \left[1 - \frac{\chi}{\hat{\chi}} \right] + \kappa \rho(T) e^{-\beta/\chi} \left[1 - \frac{\chi}{\theta} \right] \right\} + l^2 \frac{2}{\tau_0} f(s) e^{-1/\chi} \frac{\partial^2 \chi}{\partial y^2}. \quad (\text{A7})$$

APPENDIX B: ANALYSIS OF THE DYNAMIC LENGTH SCALE \mathcal{L}

The dynamic length scale that governs the initial rate of band broadening and is defined as:

$$\mathcal{L} = 4\sqrt{2} l e^{1/\hat{\chi}} \sqrt{a e^{-1/\chi_0}}. \quad (\text{B1})$$

In this expression l is a length scale on the order of an STZ radius, $\hat{\chi}$ is a steady-state value of the dimensionless disorder temperature found inside the shear band, and χ_0 is the disorder temperature of material outside the band. The parameter α is a rate factor that couples shear-induced disordering to instability growth with the form:

$$\alpha = \frac{2}{\tilde{c}_0} \left(1 + \frac{1}{\chi_0} - \frac{1}{\hat{\chi}} - 2 \frac{\chi_0}{\hat{\chi}} \right) e^{-1/\chi_0}, \quad (\text{B2})$$

where \tilde{c}_0 is a dimensionless specific heat on the order of unity.

The dynamic length scale dominates the response when the shear band width is significantly smaller than its steady-state value, i.e., when $w \ll w_\infty$. This length scale was introduced as an empirical parameter in the SBSR model but is now defined using ET-STZ theory.

We examine the behavior of \mathcal{L} as a function of the structural state of the jammed material, χ_0 . Combining Eqs. (B1) and (B2) yields

$$L = 8l \exp\left(\frac{1}{\hat{\chi}} - \frac{1}{\chi_0}\right) \sqrt{\frac{1 + \frac{1}{\chi_0} - \frac{1}{\hat{\chi}} - 2 \frac{\chi_0}{\hat{\chi}}}{\tilde{c}_0}}. \quad (\text{B3})$$

The exponential term is the proportion of STZs within the jammed material at the maximum allowed disorder due to amorphous packing and approaches 1 as $\chi_0 \rightarrow \hat{\chi}$. As the jammed material becomes more disordered, the radical term decreases, suggesting a reduction in the energy dissipated into the configurational degrees of freedom. The combined effect is a dynamic length scale which increases the shear band growth rate when the state of jammed material is more disordered up to some critical value $\chi_0 \rightarrow \chi_c$. At even higher levels of disorder the shear band growth rate sharply decreases until reaching zero at the degree of disordering above which shear bands never form. The functional form of \mathcal{L} thus suggests that shear bands typically broaden faster in systems with more disordered states.

APPENDIX C: ANALYSIS OF THE SHEAR BAND SATURATION LENGTH SCALE, w_∞

Transient shear bands are expected to broaden to a limiting width, as defined by the saturation length scale:

$$w_\infty = \frac{1}{2} \frac{a}{\tilde{\kappa}} \tau_0 V e^{1/\hat{\chi}}. \quad (\text{C1})$$

In this expression τ_0 is a material timescale on the order of the Einstein period, V is the rate of deformation imposed on the system, $\hat{\chi}$ is a steady-state value for the dimensionless effective temperature, and α and κ are rate factors for instability growth due to mechanical work and thermal fluctuations, respectively.

As the width of the shear band approaches the saturation length scale the rate of shear band broadening goes to zero. The saturation width depends both on a and $\tilde{\kappa}$, which suggests it is set by a competition between stress-induced structural rejuvenation and thermal relaxation.

We expand Eq. (C1), substituting expressions for α [Eq. (B2)] and $\tilde{\kappa}$ [Eq. (11)]:

$$w_\infty = \frac{\tau_0 V}{\epsilon_0 \kappa \rho(T)} \left(\frac{1 + \frac{1}{\chi_0} - \frac{1}{\hat{\chi}} - 2 \frac{\chi_0}{\hat{\chi}}}{2 \frac{\chi_0}{\theta} + \frac{\beta}{\theta} - \frac{\beta}{\chi_0} - 1} \right) \exp \left(\frac{1}{\hat{\chi}} - \frac{1}{\chi_0} + \frac{\beta}{\chi_0} \right). \quad (\text{C2})$$

The term in the parenthesis decreases as the effective temperature of the jammed state, χ_0 , increases, once again demonstrating that thermal relaxation dampens the effects of shear induced disordering resulting in the reduction of the saturation length scale. The exponential term, by contrast, represents the fraction of STZs available to deform, which increases with effective temperature. The combined effect is a saturation length scale that is small for less disordered systems with low effective temperatures but which increases exponentially for systems whose disorder temperature approaches the steady-state value.

-
- [1] A. R. Hinkle and M. L. Falk, *J. Rheol.* **60**, 873 (2016).
 [2] M. Oda, T. Takemura, and M. Takahashi, *Géotechnique* **54**, 539 (2004).
 [3] R. Maaß and J. F. Löffler, *Adv. Funct. Mater.* **25**, 2353 (2015).
 [4] M. L. Falk and J. S. Langer, *Annu. Rev. Condens. Matter Phys.* **2**, 353 (2011).
 [5] M. M. Trexler and N. N. Thadhani, *Prog. Mater. Sci.* **55**, 759 (2010).
 [6] E. A. Jagla, *J. Stat. Mech.* (2010) P12025.
 [7] P. G. Wolynes, *Proc. Natl. Acad. Sci. USA* **106**, 17247 (2009).
 [8] D. Vandembroucq and S. Roux, *Phys. Rev. B* **84**, 134210 (2011).
 [9] A. Wisitsorasak and P. G. Wolynes, *Proc. Natl. Acad. Sci. USA* **114**, 1287 (2017).
 [10] W. van Saarloos, *Phys. Rep.* **386**, 29 (2003).
 [11] J. S. Langer, *Phys. Rev. E* **77**, 021502 (2008).
 [12] Y. Fan, T. Iwashita, and T. Egami, *Nat. Commun.* **8**, 15417 (2017).
 [13] M. Zink, K. Samwer, W. L. Johnson, and S. G. Mayr, *Phys. Rev. B* **73**, 172203 (2006).
 [14] M. L. Falk and J. S. Langer, *Phys. Rev. E* **57**, 7192 (1998).
 [15] J. S. Langer, *Phys. Rev. E* **70**, 041502 (2004).
 [16] M. L. Manning, E. G. Daub, J. S. Langer, and J. M. Carlson, *Phys. Rev. E* **79**, 016110 (2009).
 [17] S. Plimpton, *J. Comput. Phys.* **117**, 1 (1995).
 [18] F. Lançon, L. Billard, and P. Chaudhari, *Europhys. Lett.* **2**, 625 (1986).
 [19] H. W. Sheng, M. J. Kramer, A. Cadien, T. Fujita, and M. W. Chen, *Phys. Rev. B* **83**, 134118 (2011).
 [20] F. H. Stillinger and T. A. Weber, *Phys. Rev. B* **31**, 5262 (1985).
 [21] Y. Shi, M. B. Katz, H. Li, and M. L. Falk, *Phys. Rev. Lett.* **98**, 185505 (2007).
 [22] W. G. Hoover, *Phys. Rev. A* **31**, 1695 (1985).
 [23] J. Ding, S. Patinet, M. L. Falk, Y. Cheng, and E. Ma, *Proc. Natl. Acad. Sci. USA* **111**, 14052 (2014).
 [24] C. Fusco, T. Albaret, and A. Tanguy, *Phys. Rev. E* **82**, 066116 (2010).
 [25] J. Tersoff, *Phys. Rev. B* **38**, 9902 (1988).
 [26] D. J. Evans and G. P. Morriss, *Phys. Rev. A* **30**, 1528 (1984).
 [27] P. J. Davis and B. D. Todd, *J. Chem. Phys.* **124**, 194103 (2006).
 [28] A. W. Lees and S. F. Edwards, *J. Phys. C* **5**, 1921 (1972).
 [29] A. Stukowski, *Model. Simul. Mater. Sci. Eng.* **18**, 015012 (2010).
 [30] I. Amidror, *J. Electron. Imaging* **11**, 157 (2002).
 [31] C. Liu, V. Roddatis, P. Kenesei, and R. Maaß, *Acta Mater.* **140**, 206 (2017).